Magnetic profile of proximity-coupled $(Dy,Bi)_2Te_3/(Cr,Sb)_2Te_3$ topological insulator heterostructures

L. B. Duffy,[1,2] N.-J. Steinke,[2] D. M. Burn,[3] A. Frisk,[3] L. Lari,[4,5] B. Kuerbanjiang,[1,4] V. K. Lazarov,[4] G. van der Laan,[3] S. Langridge,[2] and T. Hesjedal[1,*]

[1]*Department of Physics, Clarendon Laboratory, University of Oxford, Oxford OX1 3PU, United Kingdom*

[2]*ISIS, Rutherford Appleton Laboratory, Harwell Science and Innovation Campus, Science and Technology Facilities Council, Oxon OX11 0QX, United Kingdom*

[3]*Magnetic Spectroscopy Group, Diamond Light Source, Didcot OX11 0DE, United Kingdom*

[4]*Department of Physics, University of York, Heslington, York YO10 5DD, United Kingdom*

[5]*York-JEOL Nanocentre, University of York, Heslington, York YO10 5BR, United Kingdom*

(Received 17 June 2019; published 1 August 2019)

Magnetic topological insulators (TIs) are an ideal playground for the study of novel quantum phenomena building on time-reversal symmetry-broken topological surface states. By combining different magnetic TIs in a heterostructure, their magnetic and electronic properties can be precisely tuned. Recently, we have combined high-moment $Dy:Bi_2Te_3$ with high transition temperature $Cr:Sb_2Te_3$ in a superlattice, and we found, using x-ray magnetic circular dichroism (XMCD), that long-range magnetic order can be introduced in the $Dy:Bi_2Te_3$ layers. Accompanying first-principles calculations indicated that the origin of the long-range magnetic order is a strong antiferromagnetic coupling between Dy and Cr magnetic moments at the interface extending over several layers. However, based on XMCD alone, which is either averaging over the entire thin-film stack or is surface-sensitive, this coupling scenario could not be fully confirmed. Here we use polarized neutron reflectometry, which is ideally suited for the detailed study of superlattices, to retrieve the magnetization in a layer- and interface-resolved way. We find that the magnetization is, in contrast to similar recent studies, homogeneous throughout the individual layers, with no apparent interfacial effects. This finding demonstrates that heterostructure engineering is a powerful way of controlling the magnetic properties of entire layers, with the effects of coupling reaching beyond the interface region.

DOI: 10.1103/PhysRevB.100.054402

I. INTRODUCTION

Time-reversal symmetry breaking in the topological surface state of a topological insulator (TI) results in the massless Dirac fermions acquiring mass [1–3], giving rise to exotic physical phenomena such as the quantum anomalous Hall (QAH) effect [4] and axion electrodynamics [5]. Magnetic TIs, i.e., magnetically doped and long-range ordered TIs, can host these states, and the QAH has been experimentally observed in Cr- and V-doped $(Bi,Sb)_2Te_3$ [6–8]. To raise the temperature at which these effects can be observed to at least above liquid He temperatures, several alternative doping approaches have been explored [9–11], of which modulation doping, i.e., the separation of the dopant and the electronically active layer [12,13], appears to be most promising [14,15] as it reduces disorder [16]. In fact, modulation doping with Cr has led to the first successful observation of the axion insulator state [17].

However, by making use of magnetic coupling effects at layer interfaces, such as proximity coupling [18], the magnetic and electronic properties of magnetic TIs can be controlled through heterostructure engineering [19]. Proximity-coupling effects can be observed at the interface of a TI and a magnetically ordered (ferro-, ferri-, or antiferromagnetic) layer, whereby magnetic order is introduced in the magnetic TI (MTI) [20–24]. Hereby, the charge carriers in the topological surface state may or may not mediate the coupling between the local magnetic moments, and the precise study using spectroscopic techniques is essential as even the structurally well-behaved Cr-doped TI materials were found to unexpectedly exhibit covalent bonding and to be nominally divalent [25,26].

The flexibility of design in advanced heterostructure growth by molecular beam epitaxy (MBE) enables great opportunities for designing TI systems with novel properties. A recent example are antiferromagnetic CrSb/ferromagnetic Cr-doped $(Bi,Sb)_2Te_3$ superlattices in which high-temperature long-range ordering was mediated by antiferromagnetism [24]. The same approach can be used to combine the advantages of the high ordering temperature magnetic TIs with the high magnetic moments of a rare-earth-doped layer into one system. Cr-doped $(Sb,Bi)_2Te_3$ has the advantage of offering both a magnetic ordering temperature above 100 K and high crystalline quality [27]. On the other hand, doping TIs with high magnetic moment elements, such as isoelectronic $4f$ rare-earth atoms, has not led to long-range ferromagnetic

*Author to whom all correspondence should be addressed: Thorsten.Hesjedal@physics.ox.ac.uk

order [9,28,29], despite finding a gapped topological surface state band in Dy-doped Bi_2Te_3 [10]. Recently, we have demonstrated the successful growth of high-quality Dy-doped Bi_2Te_3 and Cr-doped Sb_2Te_3 magnetic TI superlattices using MBE [30]. Using x-ray absorption spectroscopy (XAS) and x-ray magnetic circular dichroism (XMCD) in surface-sensitive total-electron-yield mode and structure-averaging luminescence yield mode, we investigated the near-surface and integrated chemical and magnetic properties of these heterostructures. We found that ferromagnetic order can be imprinted into the otherwise paramagnetic Dy:Bi_2Te_3 layers ($T_C^{Cr} \approx 17$ K) by the proximity to Cr:Sb_2Te_3 ($T_C^{Cr} \approx 70$ K) [30]. By using first-principles calculations, we found an enhancement of the magnetic interaction in the vicinity of the interface, which extends over several atomic layers.

Here we present a study of the magnetic and structural properties of magnetic TI heterostructures consisting of five transition-metal-doped $(Cr,Sb)_2Te_3$ and rare-earth-doped $(Dy,Bi)_2Te_3$ bilayers. Using polarized neutron reflectometry (PNR), we are able to retrieve the magnetization in a layer-resolved way. We find that the magnetization is homogeneous throughout the layers, with no apparent interfacial effects, and that the magnetic behavior of the Dy-doped layers is distinctly different form single-layer thin films of the same material [31]. This demonstrates that the magnetic properties of individual layers can be fully engineered in a heterostructure, exceeding interfacial effects alone.

II. EXPERIMENTAL METHODS

The heterostructure samples, consisting of Cr- and Dy-doped bilayer repeats, were MBE-grown on Al_2O_3 (0 0 0 1) substrates using the same process as outlined in Ref. [30]. An initial layer of Bi_2Te_3 was deposited at a temperature of 200 °C and annealed in a Te environment for 30 min at a substrate temperature of 250 °C [32]. The magnetically doped layers were then subsequently deposited at a substrate temperature of 250 °C [9,25,33,34]. Dy-doped Bi_2Te_3 was deposited first on top of the Bi_2Te_3 seed layer, followed by a Cr-doped Sb_2Te_3 layer. In total, the sample consists of $n = 5$ bilayers of $(Dy,Bi)_2Te_3$ and $(Cr,Sb)_2Te_3$. The sample was subsequently capped with Bi to protect its surface from oxidation. *In situ* reflection high-energy electron diffraction (RHEED) was carried out on selected samples to monitor the quality of the layer stack at various stages during growth. Typical examples for the superlattice series can be found in Ref. [30].

X-ray-reflectometry (XRR) and -diffraction (XRD) measurements were carried out using Cu $K\alpha_1$ radiation in order to determine film thicknesses and interfacial roughnesses, as well as to determine the crystalline quality of the superlattices. High-angle annular dark-field scanning transmission electron microscopy (HAADF-STEM) data were acquired in a 200 kV JEOL 2200FS microscope and equipped with imaging and probe aberration correctors. For the specimen preparation for cross-sectional imaging, a focused ion beam system (FEI Nova 200 NanoLab) was used. Before preparing the specimen, a thin layer of carbon was deposited on top of the sample, followed by ∼10 nm of PtPd, to protect it from Ga ion implantation and ion damage.

A superconducting quantum interference device (SQUID) vibrating sample magnetometer (VSM) was used to investigate the bulk magnetic properties of the samples. The in-plane magnetization of the sample was recorded as the temperature was increased from 1.8 K up to 300 K in an applied field of 2 mT (after field-cooling at that field value). Hysteresis loops were measured with in-plane applied magnetic fields of up to 5 T at a number of temperatures ranging from 5 to 150 K.

Polarized neutron reflectometry (PNR) measurements without polarization analysis were obtained at the Offspec beamline at the ISIS neutron and muon source (Rutherford Appleton Laboratory, UK). The measurements were carried out at 3, 30, and 300 K in both a low (0.02 T) and high (0.65 T) magnetic field that is applied in-plane, parallel to the polarization axis of the neutrons. This measurement setup allows the determination of the structural depth profile as well as the depth profile of the magnetization component parallel to the applied field in the plane of the sample. While resolving the depth profile with subnanometer resolution in the direction parallel to the surface normal, the technique averages the structural and magnetic profile within the plane of the sample and is also not sensitive to the out-of-plane component of the magnetization [35]. The reflectivity curves were fitted using the GenX package [36]. Models were obtained by parallel fitting all data sets for the high fields and low fields, respectively. For the low-field measurements, the structural data from the high-field measurements were used and only the magnetization was allowed to vary.

To minimize the number of free parameters in the model, the doping concentrations and densities were assumed to be the same for each layer type. In addition, the magnetic moment was assumed to be the same for each layer type at a given temperature and field, though more free models were also tried. Attempts to assume a constant layer thickness for each layer type did not yield a satisfactory fit and therefore the layer thicknesses and roughnesses were treated as independent variables. As a further constraint, the total magnetization at 30 K was fixed to be 74% of the total magnetization at 3 K as determined by the SQUID hysteresis loops at the relevant temperatures. This constraint helped to limit the amount of cross correlation present between the magnetic moment and doping concentrations in the doped layers. In addition, the measurement at 300 K, where no magnetic component is present in the film, also helps to limit this correlation. Errors are given as 5% variation in the figure of merit, here χ^2, and they have been estimated in GenX.

III. RESULTS

A. Structural properties

Figure 1(a) shows out-of-plane XRD measurements with the (0 0 3l) film reflections labeled, along with the substrate peaks. The XRD measurements are consistent with previously published data of the underlying single-layer systems [30,37]. The data show superlattice peaks, indicating a well-defined multilayer structure with smooth interfaces. From the positions of the Bragg and satellite peaks, the bilayer and total layer thicknesses can be obtained, which are consistent with

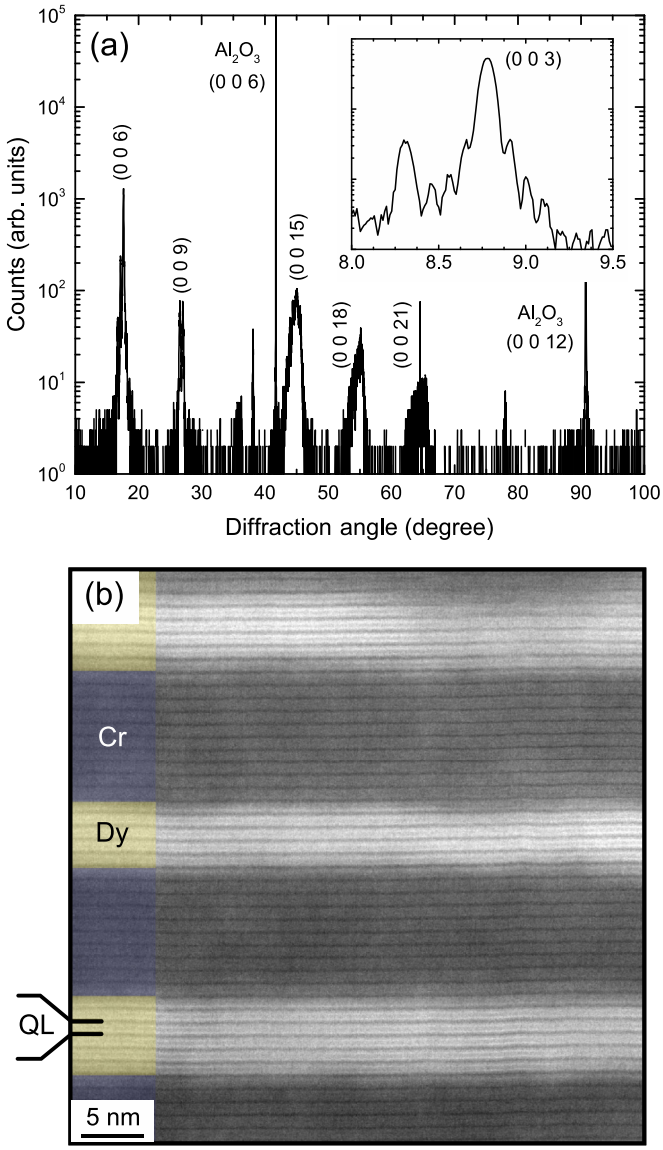

FIG. 1. (a) X-ray diffraction measurement (2θ-ω scan) of the $[(Dy,Bi)_2Te_3/(Cr,Sb)_2Te_3]_5$ MTI heterostructure grown on c-plane sapphire. The (0 0 3l) families of layer-related peaks, as well as the substrate peaks, are labeled in the figure. The inset shows the scan around the (0 0 3) Bragg peak together with the intense bilayer satellite peak, between which additional peaks consistent with the $n = 5$ bilayer structure are found. (b) HAADF-STEM image of a similar $n = 5$ heterostructure (with slightly different layer thicknesses). The thinner $(Dy,Bi)_2Te_3$ layer and the thicker $(Cr,Sb)_2Te_3$ layer are labeled. A quintuple layer (QL), consisting of Te-Bi-Te-Bi-Te, is indicated in the figure.

the XRR measurements (not shown). The observation of three peaks between the main Bragg peak and the satellite peak confirms the number of five bilayer repeats.

Polarized neutron reflectometry measurements were carried out at various temperatures and fields. Measurements were also carried out at room temperature, where no magnetic contributions are present. This allows for the determination of the Cr- and Dy-doping concentrations for each of the bilayers. The doping concentrations are found to be consistent throughout the stack, with a Dy concentration of $x = 0.393 \pm 0.002$ (in $Dy_xBi_{2-x}Te_3$) and a Cr concentration of $y = 0.47 \pm 0.05$ (in $Cr_ySb_{2-y}Te_3$). One exception is the first bilayer, for which a slightly reduced Dy concentration of $x_{BL1} = 0.3$ was found. These doping concentrations are consistent with the values for previously grown single layers, for which Rutherford backscattering was used to determine the concentrations [9,34]. Figure 1(b) shows a TEM image of a five-bilayer superlattice of alternating Dy- and Cr-doped TI layers. Due to the Z dependence of the contrast in HAADF imaging, the Dy-doped layers are brighter compared to Cr-doped layers, hence they can be clearly distinguished.

B. Magnetic characterization

Figure 2(a) shows the temperature dependence of the magnetization, $M(T)$, and panel (b) shows the first derivative, dM/dT. The measurement was taken in an applied in-plane field of 2 mT. The minima of dM/dT indicate magnetic transitions of the sample. Two transition temperatures are found, one at 36 K and another at 70 K. No meaningful data could be obtained for the derivative below 25 K. These temperatures correspond to the magnetic transition temperatures, T_C, of the Dy- and Cr-doped layers contained within the heterostructure, respectively. Arrott plots generated from element-specific XMCD hysteresis loops on similar layer stacks have revealed $T_C^{Dy} = 17$ K and $T_C^{Cr} = 70$ K for the Dy- and Cr-doped layers, respectively [30]. While the T_C^{Cr}'s obtained by SQUID magnetometry and XMCD-based Arrott plots [38] are in good agreement, the T_C^{Dy}'s differ by 19 K. However, this discrepancy may be due to the complexity of the T_C^{Dy} estimate due to the occurrence of magnetic disorder in the Dy-doped layer [30,31], which necessitates a temperature-dependent Arrott analysis [39].

Figure 2(c) shows $M(H)$ hysteresis loops with the field applied in-plane, measured at increasing temperatures from 5 to 150 K. The magnetization curves are dominated by the properties of the $(Cr,Sb)_2Te_3$ layers, and they generally exhibit the same behavior as single-layer $(Cr,Sb)_2Te_3$, for which the easy axis of magnetization is out-of-plane [see Fig. 4(a) in Ref. [34]]. Open hysteresis loops with a remanent magnetization are found for temperatures of up to ∼30 K, with coercive fields of ∼20 mT at 5 K, shown in the inset to Fig. 2(c).

Figure 3(a) shows the polarized neutron reflectivity data for the spin-up and spin-down channels, obtained in an applied magnetic field of 0.65 T and at a temperature of 3 K. The corresponding spin asymmetry, along with that obtained at 30 K, are shown in Fig. 3(b). A small Bragg peak at $Q \approx 0.037$ Å^{-1} is caused by the superlattice structure of the sample. Model fitting was carried out, and the best-fit results are also shown in Fig. 3. Initially, a fit model was tried in which all bilayers were kept identical throughout the superlattice, but we were unable to achieve a good quality fit with this approach. Instead, in the presented models the thicknesses were allowed to vary slightly between successive layers. In our best fits, the magnetization throughout the TI layers is homogeneous for both the Cr:TI and Dy:TI layers. From the model fit, the Bi_2Te_3 seed layer has a thickness of ∼64 Å,

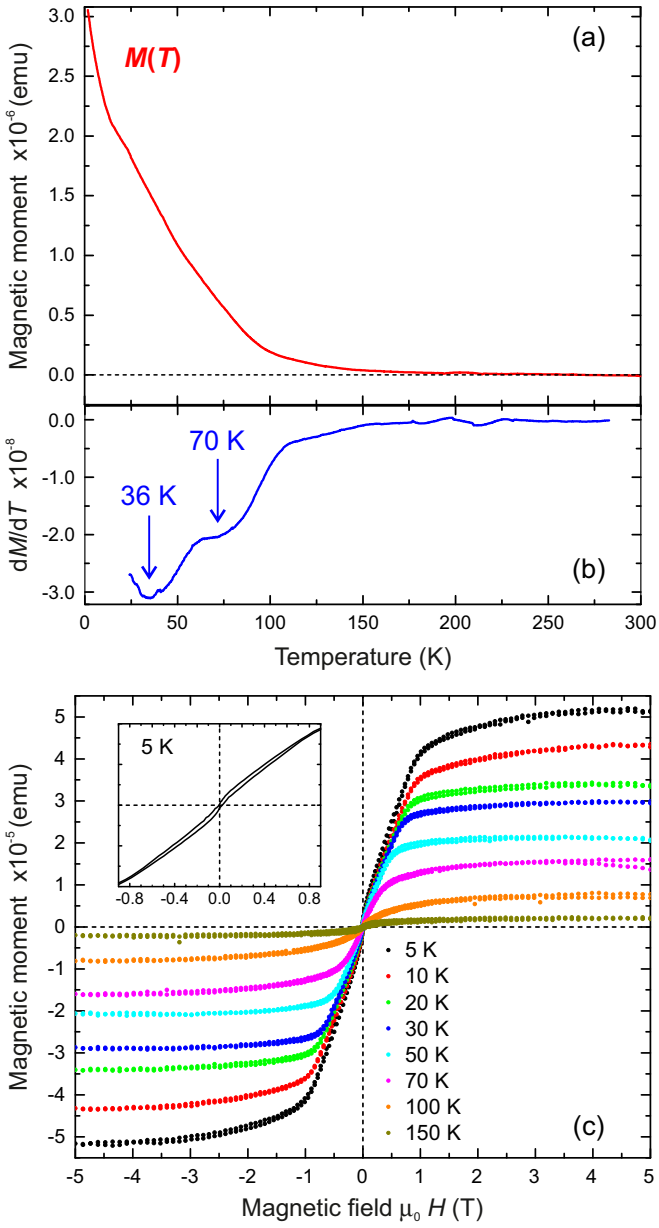

FIG. 2. Measurement of the temperature dependence of the in-plane magnetization by SQUID magnetometry. (a) $M(T)$ in an applied in-plane field of 2 mT, and (b) its first derivative dM/dT. The minima indicate two magnetic transitions in the sample at 36 and 70 K. (c) $M(H)$ magnetization loops (field applied in-plane) for a range of temperatures. The inset shows the small-field open-loop behavior of the measurement at 5 K.

a roughness of ∼10 Å, and it has no magnetic contribution, suggesting that the dopants have not significantly diffused into this layer. The Bi cap has a thickness of ∼45 Å with a large roughness and smoothly varying scattering length density, which is also slightly increased from the bulk value. This suggests that the cap is significantly oxidized. However, the unaltered properties of the layer underneath imply that the cap was able to protect the rest of the stack.

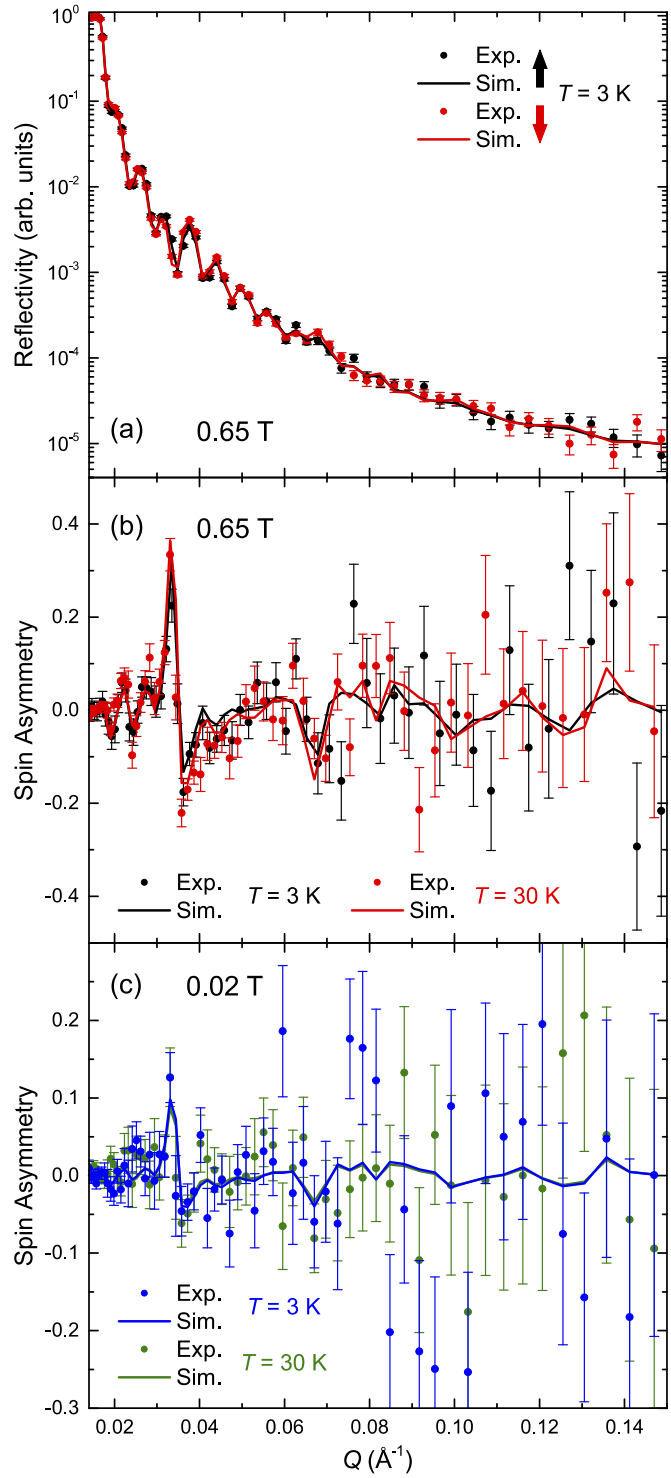

FIG. 3. PNR data and associated fits for the MTI heterostructure sample. (a) Spin-up (black) and spin-down (red) reflectivities measured at 3 K in an in-plane magnetic field of 0.65 T. (b) Spin asymmetries obtained at 3 K (red circles) and 30 K (black circles) in applied magnetic fields of 0.65 T with accompanying fits (solid lines). (c) Spin asymmetries and associated fits obtained in lower applied magnetic fields of 0.02 T at temperatures of 3 K (blue) and 30 K (green), respectively.

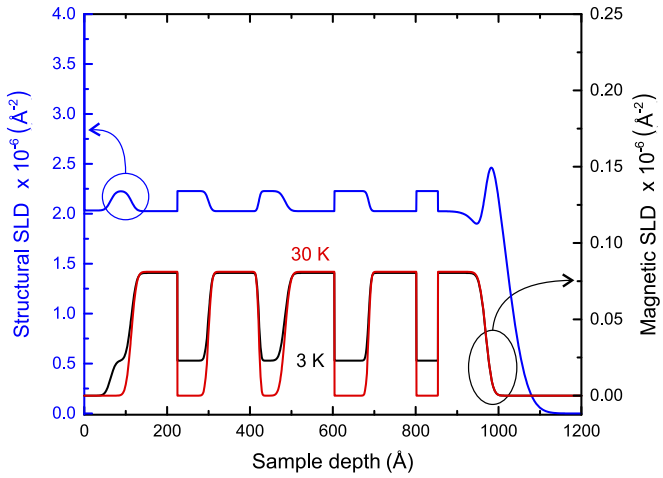

FIG. 4. Simulated best-fit structural (blue, left axis) and magnetic (right axis) scattering length densities (SLDs) as a function of depth for the 0.65 T data. The black curve represents the magnetic SLD for the 3 K data and the red for the 30 K data. At depth 0 Å, the substrate-seed layer interface is located, and the Bi cap starts at ∼1000 Å.

The first grown bilayer has a slightly reduced thickness with a $(Dy,Bi)_2Te_3$ thickness of 50 Å and a $(Cr,Sb)_2Te_3$ thickness of 111 Å. Subsequent layers are structurally quite similar with $(Dy,Bi)_2Te_3$ layer thicknesses ranging from 63 to 82 Å and $(Cr,Sb)_2Te_3$ thicknesses ranging from 115 to 121 Å. In the top bilayer, the $(Dy,Bi)_2Te_3$ layer thickness is slightly reduced to 52 Å. The uncertainty estimated on the layer thicknesses does not exceed 3 Å. Roughnesses on the Å scale are observed for the layer interfaces, with the exception of the Bi cap, consistent with the TEM results. However, detailed figure of merit scans revealed that the model is not equally sensitive to all layer roughnesses, and error bars as large as 1 nm are present in some cases. Typical roughnesses for the $(Dy,Bi)_2Te_3$ layers are 5–10 and 2–4 Å for the $(Cr,Sb)_2Te_3$ layers.

Figure 4 summarizes the structural and magnetic scattering length density profile for an applied field of 0.65 T data obtained at 3 and 30 K with well-defined interfaces between layers.

The spin asymmetries, Fig. 3(b), show a large and sharp feature around the Bragg peak position ∼0.037 $Å^{-1}$, and this region is very sensitive to the magnetic structure of the sample. We find that the spin-asymmetry amplitude around this feature is larger at 30 K compared to 3 K at the same magnetic field. The reason for this behavior is that the contrast between the Cr- and Dy-doped layers is reduced when the Dy magnetization is increased.

The contrast, determined by the bound coherent nuclear scattering length, between Sb and Cr, and especially between Bi and Dy, is considerable: $b_c^{Sb} = 5.57$ fm, $b_c^{Cr} = 3.635$ fm, $b_c^{Bi} = 8.532$ fm, and $b_c^{Dy} = 16.9$ fm. In consequence, the reflectivity measurements are sensitive to the doping concentration and there is good contrast between the Cr- and Dy-doped layers.

In all our fits, we allowed the magnetization to assume negative or positive values, allowing for the possibility of antiparallel alignment between the layers. In addition, we tried various scenarios in which the magnetization throughout the individual layers was allowed to be inhomogeneous, simulating, for instance, a magnetic proximity effect between the Cr:TI and Dy:TI interfaces. However, these fit attempts always collapsed back to a model where the magnetization was even throughout the Cr- and Dy-doped layers resolved in the direction parallel to the surface normal.

At the higher field of 0.65 T and at 3 K, each bilayer of the sample is found to have an in-plane Cr moment of $(1.03 \pm 0.01)\,\mu_B$/ion and a Dy moment of $(0.37 \pm 0.02)\,\mu_B$/ion. Increasing the temperature to 30 K causes the in-plane Dy magnetic moment to vanish. The Cr moment, based on the constraints outlined above, remains unchanged at $(1.03 \pm 0.02)\,\mu_B$/ion.

The sample was also measured at a lower field of 0.02 T at temperatures of 3 and 30 K. Figure 3(c) shows the spin asymmetries for the low-field measurements along with the corresponding model fits. As for the high-field data, the Bragg peak is still evident, however the low-field spin asymmetries are essentially temperature-independent. At 3 K, the Cr moment was found to be $\mu_{Cr} = (0.22 \pm 0.1)\,\mu_B$/ion and the Dy moment $\mu_{Dy} = (-0.06 \pm 0.15)\,\mu_B$/ion, while at 30 K, $\mu_{Cr} = (0.24 \pm 0.1)\,\mu_B$/ion and μ_{Dy} is vanishing.

IV. DISCUSSION

Recently, we reported density-functional calculations that predicted the Dy-doped layer to order ferromagnetically due to proximity coupling with the Cr-doped layer [30]. The extent of this ordering was predicted to be limited to the interface region with the center of the film remaining paramagnetic and the ferromagnetic layer to align antiferromagnetically with the Cr-doped layer. Further, we stated that in XMCD measurements the magnetic moment projected onto the direction of the incoming x-ray beam (at 54.7° to the sample surface) is parallel between the Cr and Dy moments after application of high magnetic fields of 6 T. However, XMCD is unable to resolve the magnetization profile throughout the layer and it remained unclear how much of the Dy dopants had ordered ferromagnetically. In addition, the application of very high fields made it difficult to determine the anisotropy.

To test the prediction, we allowed the magnetization to vary throughout the respective TI layers when fitting the neutron reflectometry data, but the best fits consistently were given with a homogeneous magnetization throughout the depth of each layer.

The magnetic moment per Cr atom behaves broadly in line with our expectation from single-film measurements [34]. Attempts to implement a proximity-coupled model where the Dy:TI layer is coupled to the Cr:TI layer near the interfaces and behaves similar to single-film Dy:TI layers [31] in the center of the film were unsuccessful. Instead, we find a constant magnetization throughout the Dy-doped layer that is parallel to the in-plane component of the Cr-doped layer and the applied field.

Surprisingly, the net magnetic moment per Dy ion projected onto the applied field is $0.37\,\mu_B$, much smaller than the $2.8\,\mu_B$ found in our single-layer measurements of paramagnetic Dy-doped films also using PNR [31]. This suggests that

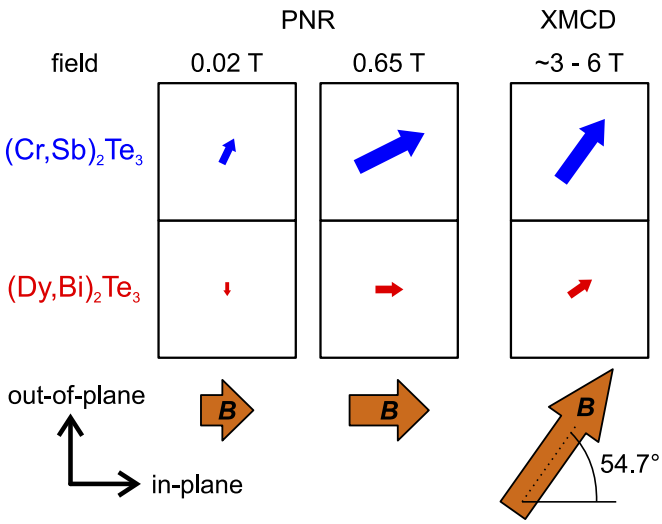

FIG. 5. Depiction of the orientation of the Cr and Dy moments in the MTI heterostructure as a function of applied field at low temperatures (∼3 K). For a low in-plane field of 0.02 T, as used in the PNR measurements, the Dy moments align antiparallel to the Cr moments, which have an out-of-plane easy axis of magnetization. At 0.65 T, the Cr moments start rotating into the in-plane direction, while the small net Dy moments are already fully aligned with the field. Note that in the PNR measurements, only the in-plane components of the magnetic moments are resolved. In the field range between ∼3 and 6 T, i.e., above the saturation field of Cr but below the saturation field of Dy, the Cr moments fully follow the applied field angle of 54.7° used for XMCD, while the Dy moments are not saturated yet.

the Dy moments are not all aligned along the *same* direction on an atomic scale. They could be, e.g., antiferromagnetically ordered, in a twisted configuration, or aligned along different orthogonal easy axes.

We summarize the configuration of the magnetic moments in the MTI heterostructure as a function of applied magnetic field in Fig. 5. Below the Curie temperature of the $(Dy,Bi)_2Te_3$ layer in the heterostructures, the Cr and Dy moments couple, most probably antiferromagnetically, across the interface at remanence (0.02 T), with their moments out-of-plane (perpendicular to the interface) dictated by the anisotropy of the Cr-doped layer. The net Dy moment is small across the layer ($\sim 0.4\mu_B$, which is 4% of the theoretical Hund's rule moment) and has weak anisotropy. Once a field is applied, the magnetic moments are gradually being pulled away from their out-of-plane orientation toward the field direction. At 0.65 T, the net Dy moment remains small and it is already fully aligned with the field. For comparison, in the XMCD measurements at high fields of 6 T, above the saturation field of the Cr moments, all Cr moments are aligned with the field, while the individual atomic Dy moments are mostly, but not completely, aligned with the field (see Fig. 3 in Ref. [30]).

V. CONCLUSION

In summary, we carried out a depth-resolved study of the magnetic properties of $[(Dy,Bi)_2Te_3/(Cr,Sb)_2Te_3]_n$ heterostructures. The sample consisting of $n = 5$ bilayer repeats has well-defined interfaces, is free from parasitic secondary phases, and shows no mixing of the two dopants Dy and Cr across the interfaces. SQUID magnetometry, consistent with XMCD, reveals two ferromagnetic transition temperatures, which can be attributed to the two magnetically distinct Dy- and Cr-doped layers. Hysteresis loops taken at several temperatures with the magnetic field applied in-plane show a hard axis behavior, i.e., the overall sample has an out-of-plane easy axis. A small remanence at temperatures below 30 K is found. PNR measurements taken in low (0.02 T) and high (0.65 T) applied magnetic field show an even magnetization profile throughout both the Cr and Dy layers. In particular, the magnetic ordering in the Dy layer is not restricted to the Cr interface as predicted by DFT calculations [30] and behaves distinctly from a single-layer Dy-doped films [31]. The very small net magnetic moment in the Dy layers, compared to their paramagnetic counterparts, suggests that a more complex spin arrangement, such as antiferromagnetic order or a twisted spin structure, may be present in these layers. PNR is ideally suited for the detailed study of such superlattices as it allows for the precise extraction not only of the magnetic film properties, but also of variation of these properties with the ultrathin films. This allows for further optimizing tailored MTI heterostructures, which hold great promise for future applications.

ACKNOWLEDGMENTS

We thank the ISIS neutron and muon source [40] for beamtime. T.H. acknowledges funding from the John Fell Fund (University of Oxford), EPSRC (EP/P020151/1), and thanks RCaH for their hospitality. L.B.D. acknowledges financial support from STFC (UK) and EPSRC (UK), and A.F. acknowledges EPSRC through Grant No. EP/P021190/1.

[1] X. L. Qi, T. L. Hughes, and S. C. Zhang, Phys. Rev. B **78**, 195424 (2008).
[2] Q. Liu, C.-X. Liu, C. Xu, X.-L. Qi, and S.-C. Zhang, Phys. Rev. Lett. **102**, 156603 (2009).
[3] Y. L. Chen, J.-H. Chu, J. G. Analytis, Z. K. Liu, K. Igarashi, H.-H. Kuo, X. L. Qi, S.-K. Mo, R. G. Moore, D. H. Lu, M. Hashimoto, T. Sasagawa, S. C. Zhang, I. R. Fisher, Z. Hussain, and Z. X. Shen, Science **329**, 659 (2010).
[4] R. Yu, W. Zhang, H.-J. Zhang, S.-C. Zhang, X. Dai, and Z. Fang, Science **329**, 61 (2010).
[5] R. Li, J. Wang, X.-L. Qi, and S.-C. Zhang, Nat. Phys. **6**, 284 (2010).
[6] C.-Z. Chang, J. Zhang, X. Feng, J. Shen, Z. Zhang, M. Guo, K. Li, Y. Ou, P. Wei, L.-L. Wang, Z.-Q. Ji, Y. Feng, S. Ji, X. Chen, J. Jia, X. Dai, Z. Fang, S.-C. Zhang, K. He, Y. Wang, L. Lu, X.-C. Ma, and Q.-K. Xue, Science **340**, 167 (2013).

[7] C.-Z. Chang, W. Zhao, D. Y. Kim, H. Zhang, B. A. Assaf, D. Heiman, S.-C. Zhang, C. Liu, M. H. W. Chan, and J. S. Moodera, Nat. Mater. **14**, 473 (2015).

[8] X. Kou, L. Pan, J. Wang, Y. Fan, E. S. Choi, W.-L. Lee, T. Nie, K. Murata, Q. Shao, S.-C. Zhang, and K. L. Wang, Nat. Commun. **6**, 8474 (2015).

[9] S. E. Harrison, L. J. Collins-McIntyre, S.-L. Zhang, A. A. Baker, A. I. Figueroa, A. J. Kellock, A. Pushp, S. S. P. Parkin, J. S. Harris, G. van der Laan, and T. Hesjedal, J. Phys.: Condens. Matter **27**, 245602 (2015).

[10] S. E. Harrison, L. J. Collins-McIntyre, P. Schönherr, A. Vailionis, V. Srot, P. A. van Aken, A. J. Kellock, A. Pushp, S. S. P. Parkin, J. S. Harris, B. Zhou, Y. L. Chen, and T. Hesjedal, Sci. Rep. **5**, 15767 (2015).

[11] L. B. Duffy, A. I. Figueroa, G. van der Laan, and T. Hesjedal, Phys. Rev. Mater. **1**, 064409 (2017).

[12] R. Dingle, H. L. Störmer, A. C. Gossard, and W. Wiegmann, Appl. Phys. Lett. **33**, 665 (1978).

[13] H. L. Störmer, A. Pinczuk, A. C. Gossard, and W. Wiegmann, Appl. Phys. Lett. **38**, 691 (1981).

[14] X. Kou, L. He, M. Lang, Y. Fan, K. Wong, Y. Jiang, T. Nie, W. Jiang, P. Upadhyaya, Z. Xing, Y. Wang, F. Xiu, R. N. Schwartz, and K. L. Wang, Nano Lett. **13**, 4587 (2013).

[15] M. Mogi, R. Yoshimi, A. Tsukazaki, K. Yasuda, Y. Kozuka, K. S. Takahashi, M. Kawasaki, and Y. Tokura, Appl. Phys. Lett. **107**, 182401 (2015).

[16] I. Lee, C. K. Kim, J. Lee, S. J. L. Billinge, R. Zhong, J. A. Schneeloch, T. Liu, T. Valla, J. M. Tranquada, G. Gu, and J. C. S. Davis, Proc. Natl. Acad. Sci. USA **112**, 1316 (2015).

[17] M. Mogi, M. Kawamura, R. Yoshimi, A. Tsukazaki, Y. Kozuka, N. Shirakawa, K. S. Takahashi, M. Kawasaki, and Y. Tokura, Nat. Mater. **16**, 516 (2017).

[18] C. Lee, F. Katmis, P. Jarillo-Herrero, J. S. Moodera, and N. Gedik, Nat. Commun. **7**, 12014 (2016).

[19] T. Hesjedal and Y. Chen, Nat. Mater. **16**, 3 (2016).

[20] P. Wei, F. Katmis, B. A. Assaf, H. Steinberg, P. Jarillo-Herrero, D. Heiman, and J. S. Moodera, Phys. Rev. Lett. **110**, 186807 (2013).

[21] M. Lang, M. Montazeri, M. C. Onbasli, X. Kou, Y. Fan, P. Upadhyaya, K. Yao, F. Liu, Y. Jiang, W. Jiang, K. L. Wong, G. Yu, J. Tang, T. Nie, L. He, R. N. Schwartz, Y. Wang, C. A. Ross, and K. L. Wang, Nano Lett. **14**, 3459 (2014).

[22] W. Yang, S. Yang, Q. Zhang, Y. Xu, S. Shen, J. Liao, J. Teng, C. Nan, L. Gu, Y. Sun, K. Wu, and Y. Li, Appl. Phys. Lett. **105**, 092411 (2014).

[23] Z. Jiang, C.-Z. Chang, C. Tang, P. Wei, J. S. Moodera, and J. Shi, Nano Lett. **15**, 5835 (2015).

[24] Q. L. He, X. Kou, A. J. Grutter, G. Yin, L. Pan, X. Che, Y. Liu, T. Nie, B. Zhang, S. M. Disseler, B. J. Kirby, W. Ratcliff II, Q. Shao, K. Murata, X. Zhu, G. Yu, Y. Fan, M. Montazeri, X. Han, J. A. Borchers, and K. L. Wang, Nat. Mater. **16**, 94 (2016).

[25] A. I. Figueroa, G. van der Laan, L. J. Collins-McIntyre, S.-L. Zhang, A. A. Baker, S. E. Harrison, P. Schönherr, G. Cibin, and T. Hesjedal, Phys. Rev. B **90**, 134402 (2014).

[26] A. I. Figueroa, G. van der Laan, L. J. Collins-McIntyre, G. Cibin, A. J. Dent, and T. Hesjedal, J. Phys. Chem. C **119**, 17344 (2015).

[27] Z. Zhou, Y.-J. Chien, and C. Uher, Phys. Rev. B **74**, 224418 (2006).

[28] S. E. Harrison, L. J. Collins-McIntyre, S. Li, A. A. Baker, L. R. Shelford, Y. Huo, A. Pushp, S. S. P. Parkin, J. S. Harris, E. Arenholz, G. van der Laan, and T. Hesjedal, J. Appl. Phys. **115**, 023904 (2014).

[29] S. E. Harrison, L. J. Collins-McIntyre, S. L. Zhang, A. A. Baker, A. I. Figueroa, A. J. Kellock, A. Pushp, Y. L. Chen, S. S. P. Parkin, J. S. Harris, G. van der Laan, and T. Hesjedal, Appl. Phys. Lett. **107**, 182406 (2015).

[30] L. B. Duffy, A. Frisk, D. M. Burn, N.-J. Steinke, J. Herrero-Martin, A. Ernst, G. van der Laan, and T. Hesjedal, Phys. Rev. Mater. **2**, 054201 (2018).

[31] L. B. Duffy, N.-J. Steinke, J. A. Krieger, A. I. Figueroa, K. Kummer, T. Lancaster, S. R. Giblin, F. L. Pratt, S. J. Blundell, T. Prokscha, A. Suter, S. Langridge, V. N. Strocov, Z. Salman, G. van der Laan, and T. Hesjedal, Phys. Rev. B **97**, 174427 (2018).

[32] S. E. Harrison, S. Li, Y. Huo, B. Zhou, Y. L. Chen, and J. S. Harris, Appl. Phys. Lett. **102**, 171906 (2013).

[33] L. J. Collins-McIntyre, S. E. Harrison, P. Schönherr, N.-J. Steinke, C. J. Kinane, T. R. Charlton, D. Alba-Veneroa, A. Pushp, A. J. Kellock, S. S. P. Parkin, J. S. Harris, S. Langridge, G. van der Laan, and T. Hesjedal, Europhys. Lett. **107**, 57009 (2014).

[34] L. Collins-McIntyre, L. Duffy, A. Singh, N.-J. Steinke, C. Kinane, T. Charlton, A. Pushp, A. Kellock, S. Parkin, S. Holmes, C. Barnes, G. van der Laan, S. Langridge, and T. Hesjedal, Europhys. Lett. **115**, 27006 (2016).

[35] B. P. Toperverg, Physica B **297**, 160 (2001).

[36] M. Björck and G. Andersson, J. Appl. Crystallogr. **40**, 1174 (2007).

[37] Y. Iwata, H. Kobayashi, S. Kikuchi, E. Hatta, and K. Mukasa, J. Cryst. Growth **203**, 125 (1999).

[38] A. A. Baker, A. I. Figueroa, K. Kummer, L. J. Collins-McIntyre, T. Hesjedal, and G. van der Laan, Phys. Rev. B **92**, 094420 (2015).

[39] I. Yeung, R. M. Roshko, and G. Williams, Phys. Rev. B **34**, 3456 (1986).

[40] N.-J. Steinke *et al.*, Magnetic interactions in ferromagnetic topological insulator multilayer structures, STFC ISIS Neutron and Muon Source (2018), doi:10.5286/ISIS.E.90586775.